
Experimental Analysis of X-Ray Fluorescence

A University of Birmingham Lab Report

By Benjamin Crump

MSc Physics & Technology of Nuclear Reactors

January 21, 2022.

Abstract

x-ray fluorescence spectroscopy provides a method of investigating material composition by the study of characteristic x-ray spectra. The purpose of this report is to experimentally investigate one of the underlying physical models of the Bohr model - Moseley's law. A Si(Li) semiconductor detector was used to measure spectra from a number of target materials, bombarded by various ^{241}Am -based sources. The x-rays fluoresced from the target materials are then tested against Moseley's law and a Bohr-Sommerfeld relativistic correction. Two unknown samples were then tested to determine composition using Moseley's law, one successfully. The main results were tested against the known value of the rest mass of an electron ($511 \text{ keV}/c^2$). Moseley's law gave $524.86 \text{ keV}/c^2 +/- 15.78$ and the Bohr-Sommerfeld approximation gave $505.42 \text{ keV}/c^2 +/- 7.53$. The effect of electron shielding σ is also discussed. It concludes that Moseley's law is an inaccurate representation of the data, and although the relativistic correction is astonishingly accurate, more modern fine structure theories of the atom show that the underlying assumptions of the time were false.

Acknowledgements: I would like to thank Dr. Paul Norman, Dr. David Forest, Prof. Peter Jones, and Pedro Santa Rita Alcibia for their patience and unwavering guidance during the laboratory sessions which made this report possible.

1 Introduction

x-ray spectroscopy is a method of radiation detection used to study; the inner shell phenomena of atoms, the states of highly ionised atoms, or to determine material properties. Lithium-drifted Silicon "Si(Li)" Semiconductor detectors are often used to measure x-rays of this origin. These detectors have exceptionally good energy resolution and intrinsic efficiency, although they can be cumbersome and require cryogenic cooling to operate successfully. The aim of this report is to experimentally investigate Moseley's Law using a Si(Li) detector by conducting x-ray spectroscopy utilising a number of ^{241}Am -based sources. The properties of the detector shall be investigated and the results are to be compared with known properties. Next, spectra from variable x-ray sources will be analysed and compared with Mosley's law then with a relativistic extension. Finally, an attempt is to be made to characterise two unknown material samples - providing an application to the aforementioned Moseley's law. The purpose of thus is to provide evidence and understanding of known physical phenomena - Moseley's law. The experiment equipment is located within the nuclear laboratory at the University of Birmingham. Given the evolution of the fundamentals of quantum phenomena over the past century, it is hypothesised that the legacy (but still relevant) theories on atomic structure are accurate, and still relevant in-practice. These early theories still apply in many applications and there must be a reason for this.

2 Theory

2.1 Detector Properties

To create an electron-hole pair in a semiconductor requires an average energy loss of $\sim 3\text{eV}$, which is as much as ten times less than an ion pair in a gas-based detector. Ergo, semiconductor detectors can offer better resolution over other detector types. Compared to HpGe, Si(Li) detectors fewer escape peaks and less interference events are observed from the detection of higher energy photons, meaning that Si(Li) detectors are typically the semiconductor detector of choice for detection of lower energy photons ($\sim \text{keV}$) [8]. This relation is apparent with the dependence of photoelectric absorption probability on the atomic number (Z) of the material. Which can be seen for the approximation given by Knoll [8] (Equation 1). Where exponent n varies between 4 and 5 over the energy region of interest.

$$\tau \cong \text{constant} \times \frac{Z^n}{E_\gamma^{3.5}} \quad (1)$$

The lower atomic number of silicon ($Z = 14$) means that, for typical gamma-ray energies, the cross section for photoelectric absorption is lower when compared to germanium ($Z = 32$). The full-energy peak efficiency for gamma-rays interacting silicon detectors is therefore increasingly poor in the energy region $> 30 \text{ KeV}$. Figure 1 illustrates this principle in practice for a number of radiation detectors.

The semiconductor properties of silicon tend to be favoured over germanium, the larger bandgap of silicon between the conduction and valence bands reduces the thermal leakage current at any temperature, benefiting energy resolution. For Si(Li) detectors fluctuations this leakage current at room temperature tends to be a significant contribution to noise. Low-noise applications therefore require detector cooling to reduce this affect. When voltage is applied Si(Li) detectors require cooling. However at room temperature, with no applied voltage, the migration of lithium is slow enough not to affect the performance of the detector.

It has not been possible to date to make thick silicon as pure as high purity germanium (HpGe). As such, lithium is diffused into the p-type silicon to make high thickness Si(Li) detectors with appropriate operating voltages. These lithium donors diffuse into the crystal until they exactly compensate for the acceptors, the resultant device has a planar p-i-n configuration. On one side there is a p-type (silicon) layer, on the front there is an n-type layer (lithium) and in between there is a compensated intrinsic layer of material, known as the depletion layer. The thickness of this region is fixed through fabrication so depletion does not tend to vary much with voltage. When this p-i-n structure operated in a reversed biased configuration, i.e. positive potential is applied to the n-type layer, negative charge is found in the p-type layer and a region of zero charge exists within the depletion layer. The resultant electric field tends to be constant throughout the crystal. The lifetime of the charge carriers within the depletion layer tends to be greater than the time required to collect them at either of the boundaries, the charge collection properties are desirable however high bias voltages are required (500-4000V, [8]) to collect quickly and in their full completeness. The layer thickness determines the active volume of the detector and the migration of the charges to the p-i and i-n boundaries produce the majority of the signal pulse.

The study of detector properties can itself be a lengthy and almost endless pursuit. Resolution across the energy region of interest for this detector shall be investigated. The energy resolution is simply a ratio of the full-width half maximum (FWHM) to the centroid position (μ) of the peak, expressed by Equation 2. Plotting the logarithm of the resolution ($\ln(R_E)$) against the logarithm of the centroid position ($\ln(E)$) should yield a gradient on a straight line fit of (roughly) -0.5 if the energy resolution is limited by Poisson statistics, if a gradient of -1 is found then the energy resolution is limited by noise. Full-energy peak efficiency tends to drop off significantly above $\sim 30\text{keV}$, the aforementioned plot should not include data points of peaks recorded above this threshold to attain an accurate result. Detector efficiency shall give an indication of how much of the

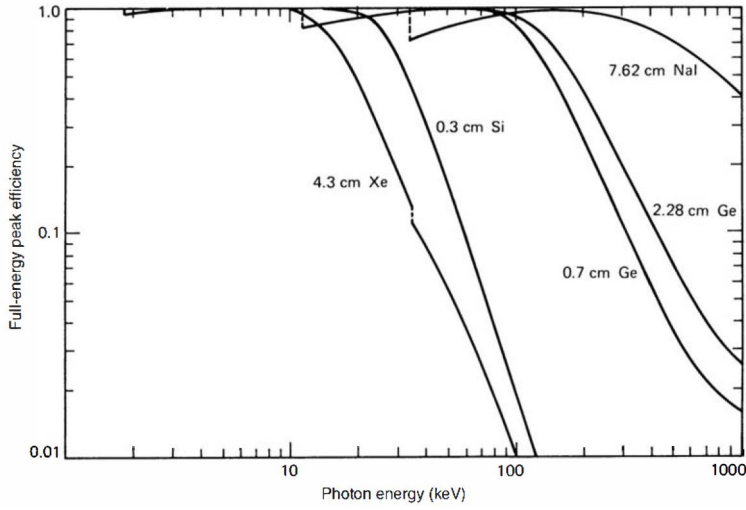


Figure 1: Full-energy peak efficiency as a function of incident photon energy for five different detector types. Thicknesses in the direction of the incident photon are also indicated on the figure [8].

incident radiation interacts with the detector. For the calculation of absolute efficiency, Equation 3 is to be followed [8]. Intrinsic efficiency, for a point source, is given by Equation 4 [8].

$$R_E = \frac{FWHM(E)}{E} \quad (2)$$

$$\epsilon_{abs} = \frac{\text{Full Energy Peak Counts / Second}}{\text{Source Activity} \times \text{Branching Ratio}} \quad (3)$$

$$\epsilon_{int} = \epsilon_{abs} \times \frac{4\pi}{\Omega}, \text{ where } \Omega = \frac{\text{Detector Frontal Plane Area (A)}}{\text{Source to Detector Distance (d}^2\text{)}} \quad (4)$$

2.2 Detector Interaction Mechanisms

A photon can interact with the silicon crystal of the detector in a number of ways, as described in detail by Knoll [8]. The relative probabilities of each interaction are shown by Figure 2. In the case of low-energy x-rays, the predominant interaction is photoelectric absorption. Incident photo-electrons ejected from the silicon atoms, excited by the incident x-rays, will conduct and produce a signal. Although peaks produced by the escape of photons may also be detected.

2.3 Characteristic x-rays

The designation "x-ray" is typically given to a photon if it is emitted to a free or bound electron and has an energy of between approximately 0.1 keV and 100 keV. A photon incident upon an atom may eject a bound electron from an atomic shell leaving behind a hole and an excited incident atom, this process is the aforementioned photoelectric absorption and occurs with probability as defined by Equation 1. The remaining bound electrons within an atom tend to arrange themselves to the lowest energy (ground) state and fill the holes, within a characteristic time period of $< ns$ for solids. The energy liberated from these electron shell transitions to the lowest energy states available take the form of characteristic x-rays, emitted with the energy difference between the initial and final states.

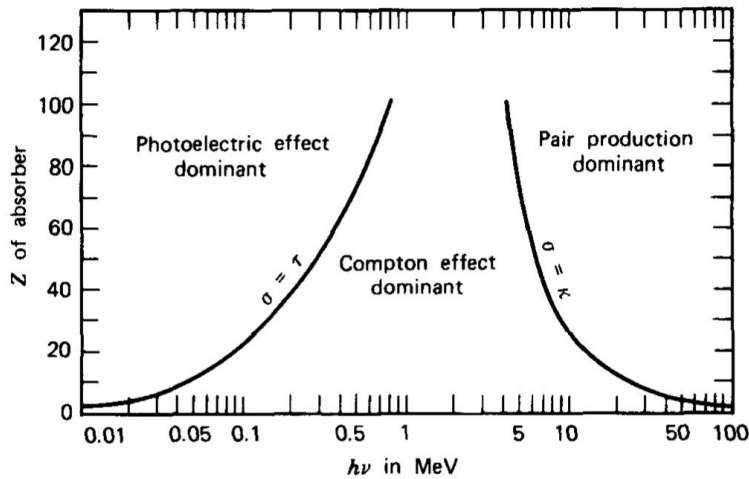


Figure 2: Relative importance of the three major photon interaction mechanisms [8].

Siegbahn	IUPAC	Siegbahn	IUPAC
$K\alpha_1$	$K - L_3$	$L\alpha_1$	$L_3 - M_5$
$K\alpha_2$	$K - L_2$	$L\alpha_2$	$L_3 - M_4$
$K\beta_1$	$K - M_3$	$L\beta_1$	$L_2 - M_4$
$K\beta_2^1$	$K - N_3$	$L\beta_2$	$L_3 - N_5$

Table 1: Siegbahn to IUPAC

x-ray lines tend to follow Siegbahn notation, developed by a physicists in the early 20th century. Although in more recent times the IUPAC notation [7] has become a more dominant notation with the initial (left) and final (right) states separated with a hyphen. Siegbahn notation is illustrated on Appendix C [1] and Table 1 provides a conversion between the two notations for a limited number of transitions. K-series x-rays tend to be the most energetic and therefore the most significant [8]. For any excited atom, the characteristic x-ray is in competition with the ejection of an Auger electron. The fraction of events where an excited atom emits a characteristic x-ray as opposed to an Auger electron is known as the fluorescent yield. The energy of a characteristic x-ray is unique to each element, therefore unknown elements may be analysed and characterised. In fact all elements can be detected with a fairly uniform sensitivity using this method. The limitations come where there are a number of K and L lines at close energies; where even Si(Li) detectors cannot resolve peaks within the scale of ~ 10 's of electron Volts (eV).

2.4 Moseley's Law

Henry Moseley was an English physicist prominent in the early 20th century, he was tragically killed in action at the age of 27 during the attack on Gallipoli in the Dardenelles (1915). One of his major achievements [6] was "Moseley's Law" which advanced the field of chemistry substantially by sorting the elements of the periodic table in a more logical manner. Finding the frequency of the lines of the characteristic x-ray spectra depended regularly on the atomic number of the relevant element, and equal to the ordinal number of the elements arranged in increasing atomic mass [4], i.e. $\sqrt{v} \propto Z$. Moseley was able to predict the existence of several unknown elements using this method, including Hafnium. The atomic number used by Moseley was later seen to equal the nuclear charge expressed in units of the absolute value of the electronic charge, or as the number of electrons on a neutral atom. These two quantities were later measured independently and each was found to equal Moseley's findings. Moseley measured and plotted around 40 elements and showed (Appendix A, Figure 21) that for the square root of the x-ray frequencies, for all lines examined, that both K and L series x-ray energies fall on an approximate straight line when plotted against their respective atomic numbers (Z). Moseley modelled this relationship [6] for both K and L series x-rays. Niels Bohr took this further

and predicted that electrons in a given shell (n) have a velocity relative to $Z\alpha c/n$ where α is the fine structure constant ($\sim 1/127$ [10]) and c is the speed of light. This relation can be used to correlate the atomic number (Z) to the energy of the given x-ray, Equation 5 illustrates where n_i is the quantum number of the initial state, n_f the final, as read off Appendix C.

Arnold Sommerfeld developed Bohr's model by making the orbits of electrons elliptical (as opposed to the previously hypothesised circular orbits) and adjusted them to fit both relativistic and non-relativistic cases. These approximations were found to be astonishingly accurate for the time. In this report, the Bohr-Sommerfeld approximations (Equations 6 - 7) [9] will be used to provide solution and comparison to Moseley's hypothesis. $m_e c^2$ should be taken as the well-known value of $511 \text{ keV}/c^2$, as retrieved from the back page of Krane [10]. According to more modern quantum mechanical models, Schrodinger's (non-relativistic) and Dirac's equation's (relativistic) would be more evolved approximations for use. Heisenberg's uncertainty principle (1926) claims that an electron (considered a wave packet) could not have an exact orbital location at an exact time, but was later found to have a probability distribution-based solution. These quantum mechanical models would be inappropriate to consider within this report and are considered as beyond the scope herein.

2.4.1 Electron Shielding (σ)

According to Moseley's Findings, for K series x-rays, a single electron in the K-shell (before emission) was assumed to be 100% effective in shielding the nucleus (denoted by σ). For transitions which start or end in higher shells, the shielding appeared to become more complex. Moseley found the best fit for L-alpha x-rays to be $Z=7.4$ which indicates that a shielding corresponding to an average of 7.4 electrons inside the M-shell (origin). However, Bohr's model predicts that for heavier elements, the innermost electrons are moving at more than half the speed of light, where relativistic corrections may start to become a factor.

For $K\alpha$ Whitaker et al [20] (1999) finds that the theoretical value of $\sigma_K \rightarrow 1$, $Z \rightarrow \infty$. As Z is greater than 10, then a σ of 1 is an appropriate approximation. This figure is also present in the approximations of Moseley [6] and Sommerfeld. For $K\beta$ an estimate of 2 shall be used, as expected with an electron transition from a higher level. Recent work by Soltis et al [18] (2017) illustrates that, with the application of modern detectors, electron shielding becomes inaccurate at higher atomic numbers and non-linear as atomic mass increases, the approximation requires first-order relativistic corrections. This shall be discussed and investigated further during the analysis of results.

$$E = m_e c^2 \alpha^2 \left(\frac{1}{n_f^2} - \frac{1}{n_i^2} \right) (Z - \sigma)^2 \quad (5)$$

$$E_{k\alpha} = m_e c^2 \left(\sqrt{1 + \alpha^2 (Z - \sigma)^2 / 4} - \sqrt{1 - \alpha^2 (Z - \sigma)^2} \right) \quad (6)$$

$$E_{k\beta} = m_e c^2 \left(\sqrt{1 + \alpha^2 (Z - \sigma)^2 / 9} - \sqrt{1 - \alpha^2 (Z - \sigma)^2} \right) \quad (7)$$

2.5 Source Decay

^{241}Am is the radioisotope (synthetic) of concern for all sources used within this experiment. It has a half life of 432.6 years and decays by $^{241}\text{Am} \rightarrow ^{237}\text{Np} + ^4\text{He}$, 100% of the time. The daughter nucleus (^{237}Np) is left in an excited state and undergoes a number of photon emissions to return to ground state. There is no need to consider beyond this herein, ^{237}Np has a half life of 2,144,000 years decaying to ^{233}Pa

3 Apparatus

3.1 Detector

The Miron technologies (Canberra) model number for this detector is SL80190. The crystal diameter is 10.1mm and the distance from the detector window to the crystal is 5mm. On top of the existing beryllium entrance window there is a silicon protective cap. According to the data sheet [12] the active area is 80mm^2 . It comes with a cryostat with a 1in. diameter, a 4in. long stainless steel end-cap and beryllium window. As previously mentioned the detector requires cooling in operation. As such there is a liquid nitrogen cryostat (dewar) located beneath the desk shown on Figure 4, this is a standard component for a number of detector types which require cooling. A general cut-away diagram (Appendix D) is provided by Miron Technologies [12]. This arrangement conducts heat away from the detector crystal and keeps the detector cooled, this ensures that the rate at which electrons are thermally excited into the conduction band of the crystal is low. The detector requires a voltage of +500V in order to sweep away conduction electrons that appear through x-ray interactions.

3.2 Electronics

Starting at the power supply unit, an ORTEC 4006 minibin and power supply [17] was used to supply electrical power to a number of modules; +6V (4A) to the ORTEC 671 amplifier and +24V (0.75A) to the NHQ 212M HV power supply. The latter [13] transforms the 24V to a voltage up to a maximum of 2kV (as selected by the potentiometer) and is then supplied to the detector.

The pre-amplifier takes the signal directly from the detector, and in this case it is mounted directly to the detector. The pre-amplifier used is a low noise integrated transistor reset pre-amplifier (gated, charge-integrating amplifier) which, when first introduced, increased throughput capabilities by a factor of 5 ensured that the pre-amplifier was no longer the limiting device in these types of set-ups. A simplified circuit diagram can be seen on Appendix D.

As the name suggests the pre-amplifier integrates the detector charge pulse, by means of capacitor C_f (Appendix D). The typical feedback resistor, usually seen on RC feedback amplifiers, is replaced with a reset circuit. The affect of thus produces a 'saw-tooth' output waveform, where the exponentially decaying tail with time constant (τ), is replaced with a straight line. However, with no feedback resistor to remove the charge from C_f between detector events, each event steps the pre-amplifier output in a 'staircase' manner until this reaches the value of power supply voltage and then resets back to the starting value. When this reset or recovery occurs an inhibit signal is produced, in order to prevent data collection. A feedback resistor also tends to be a source of thermal noise and removing it tends increase the resolution of the output pulse and improves the counting rates.

The ORTEC 671 spectroscopy amplifier (Figure 3 [15]) takes the 'staircase' output signal from the pre-amplifier and generates a series of Gaussian shaped pulses. The pulse is shaped through a series of RC and CR networks (low pass and high pass filters respectively). Where the low pass filters integrate the pulse and smooth the rising edge and the high pass filters differentiate the pulse and attenuates the tail. The result is a band pass filter which shapes the pulse into a Gaussian shape. For semiconductor detectors such as this, the shaping time (0.5 - 10 μs) can be used to minimise the electronic noise (sum of parallel and series) contribution from the pre-amplifier input, most notably the thermal noise generated by the first stage of the pre-amplifier - the field-effect transistor.



Figure 3:
ORTEC 671
amp [15].

Lower shaping times tend to benefit resolution whereas higher shaping times can severely affect the counting rates. Knoll [8] states that the use of a gated-integrator type pre-amplifier allows the use of short Gaussian shaping times, although there are a number of trade-offs for each particular detector in any given application.

There is an option for unipolar or bipolar pulse shapes, unipolar is selected in this case for improved resolution. Pole-zero adjustment is provided to cancel the undershoot which can be induced by the return to baseline of high pass filters. In this case, where a transistor-reset amplifier is used, the PZ adjustment is set fully counterclockwise (minimum) as per the ORTEC manual [15]. A pile-up rejection circuit is provided to suppress the spectral distortion caused by pulses piling up at high count rates. Baseline restoration rate can also be set to 'auto' or 'high' to prevent the baseline shifting with the amplitude of the pulses, which can degrade resolution. The high setting is used for suppressing low-frequency interference, auto matches the rate of the pole-zero position at low counting rate and increases with the counting rate [15].

The multi-channel analyser (MCA) [16] takes the stream of unipolar pulses from the amplifier and sorts them according to pulse height, of which is proportional to the energy deposited in the detector. The MCA itself is made up of banks of single channel analysers (an analogue to digital converter) which each have upper and lower level discriminators set, such that the upper level of one is the lower level of the next and so forth. This gives an output pulse for each channel for an input pulse which lands in between the upper and lower levels, producing a 'counts per channel' against channel plot. The MCA is connected to a PC which has the supplied MAESTRO software installed, when running this collects and produced the counts per channel plot when the detector is subject to an interaction.

The oscilloscope, shown above the minibin on Figure 4, is a single channel analyser (SCA) which is used during the initial set-up of the detector and associated electronics. It can be used as a check of the signals from any stage within the detector electronics chain. The majority of the detector and electronics set-up used in this experiment is illustrated on Figure 4.

3.3 Materials

In the case of this experiment, the excitation of the inner (K) shell vacancies will be performed using the 59.5 keV γ -line of a various ^{241}Am sources. Three ^{241}Am sources are to be used in this experiment, each detailed in Table 2. Data on the source activities is taken from the university virtual learning page [3].

The stick ^{241}Am source is to be used first for capturing and evaluating an ^{241}Am spectrum and investigating detector properties. The ^{241}Am variable x-ray source is to be used and the resultant K and L series x-rays are to be identified and verified against Moseley's law. This source has six select-able target materials on a rotary target wheel, detailed on Appendix B.

The final source is the high activity annular ^{241}Am source (Figure 6) which is used for the characterisation of unknown materials. This source is designed to load and secure directly into the enclosure shown on Figure 4. Inside the enclosure there are four distances which can be selected from (see Figure 4) the closest is 60mm from the detector cap and each setting increases in distance by 20mm. There are two unknown samples selected (Figure 7) which can sit on any of the four the select-able shelves. The shelf slide has a hole in the centre to allow the incident photons to pass uninhibited from the source to the sample.

Source Name	Source Ident.	Activity (Bq)	Date Measured	Ref.
^{241}Am Stick	1Q599	$397,800 \pm 19,900$	15/10/2019	N/A
^{241}Am Variable x-ray	C3N 19/35	370,000,000	Manuf. Unknown	Fig.5
^{241}Am Annular	ANS46	1,120,000,000	15/10/2019	Fig.6

Table 2: Table of sources



Figure 4: Experimental Apparatus



Figure 5: Amersham international ^{241}Am variable x-ray source.



Figure 6: Annular ^{241}Am x-ray source.



Figure 7: unknown samples "u1" and "foil" (L-R).

4 Method

4.1 Measurements

The equipment was interconnected as described by the Figure 8. The minibin and HV power supply were turned on and a HV bias of 500V was applied slowly, as specified by a label on the detector cryostat. This voltage was deemed a sensible starting point, given the recommendations of Knoll [8]. The oscilloscope was used to check the waveform at the output of the 671 and 'saw-tooth' output of the pre-amplifier. Maestro was then opened and initialised on the PC.

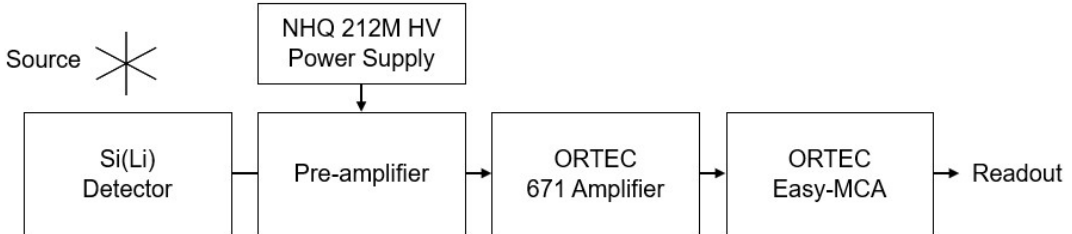


Figure 8: Interconnections block diagram.

4.1.1 ^{241}Am 1Q599 Stick Source Spectrum

The 1Q599 ^{241}Am source was placed at 60mm from the detector window, ensuring that the source has a clear line of sight to the window. An indication that this distance is suitable is provided by the PUR LED on the 671 amplifier, which appeared green indicating that 0-40% of pulses were being rejected through pulse pile-up.

The gain of the 671 amplifier was adjusted so that the 59.5 keV γ line falls in the upper portion of the Maestro spectrum, as far right on the capture as possible but still identifiable. A shaping time of $0.5 \mu\text{s}$ was selected, as explained previously in section 3.2. Baseline rejection (BLR) was set to high, given that the P-Z was set fully counterclockwise, it seemed that there was a source of unknown low-frequency noise which was reduced by selecting this setting. From the aforementioned procedure, the settings in Table 3 were selected on the 671 amplifier.

Setting	Value	Setting	Value
Bias Voltage	500V	Shaping Time	$0.5 \mu\text{s}$
Coarse Gain	100	Fine Gain	0

Table 3: 671 Amplifier Settings

The spectrum was recorded, a live time of 300 seconds gave at least 1000 counts in each peak and seemed a sensible record time to continue with. This spectrum was then saved in the ASCII format (.Spe), opening this file as a .txt file allows the data to be extracted, pasted into MS Excel, and then plotted. The spectrum obtained (Figure 9) was then labelled using the same plot within Knoll [8] (Figure 13.13 therein). The ^{237}Np M series x-rays do not seem to be present as is the case with the Knoll [8] plot, these could be masked within the unknown low-energy noise spanning from channels ~ 50 to ~ 300 . The ^{237}Np Ll line is not well resolved either and could be the slight increase in counts at around channel 270 or hidden within the tail of the combined $L\alpha 1$ 13.9 keV peak, which also contains the low intensity $L\alpha 2$ peak. The witnessed Lt and Ls peaks proposed within H.R.Verma [19] also cannot be resolved at low energies, although the relative intensities are much less than that of the aforementioned Ll line. The $L\beta$ line clearly contains three peaks, however they remain largely unresolved with only two fit-able. A number of $L\gamma$ peaks are possibly hidden within a single peak at around 21 keV, although they could not be resolved. A small bump between the ^{237}Np $L\gamma 1$ and ^{241}Am γ possibly indicate K series x-rays from the Ln and Sn detector contacts, although there are not enough counts in this region to

confirm this. Both of the ^{241}Am γ peaks are then present at higher energies, the highest 59.5 keV peak will likely have suffered from a lowered full-energy peak efficiency, as illustrated by Figure 1.

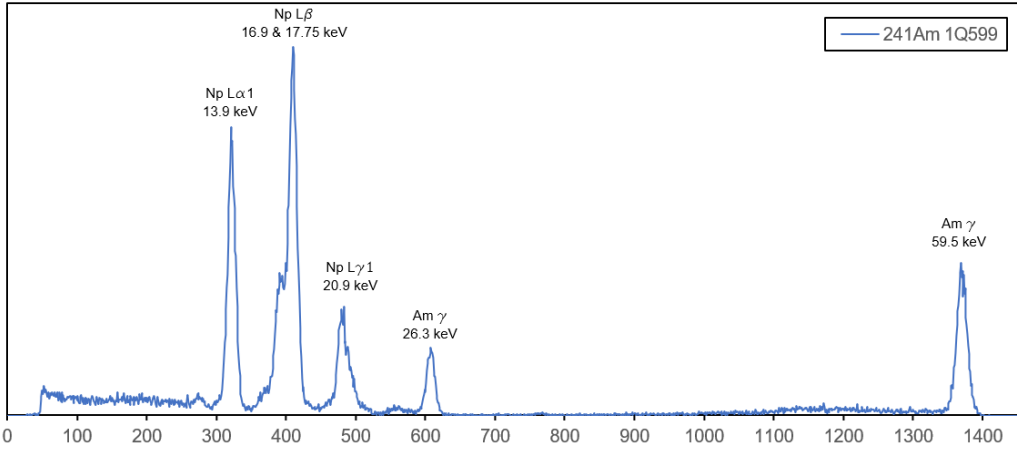


Figure 9: ^{241}Am 1Q599 spectrum plot (channel number on x-axis)

4.1.2 ^{241}Am Variable x-ray Source

The stick source was removed from the enclosure and the variable x-ray source (Figure 5) was inserted, making sure that there was line of sight between source and detector. The same detector settings as stated in Table 3 were applied, the 59.5 keV γ line still fell within the upper portion of the Maestro spectrum and the gain setting remained suitable. A single spectrum was captured for each of the six target materials detailed on Appendix B. All six spectra were saved in the ASCII format for further processing. The ASCII files were opened and plotted on MS Excel, a single 'stacked' plot was produced which displays all six spectra side-by-side (Figure 10).

The 59.5 keV γ line is present on all recorded spectra, with a low number of counts however. The $K\alpha$ and $K\beta$ lines listed on Appendix B are all present on each recorded spectrum, an energy calibration is required to identify the other peaks present. It can be seen that the energies of the peaks match the energy order as described by Appendix B.

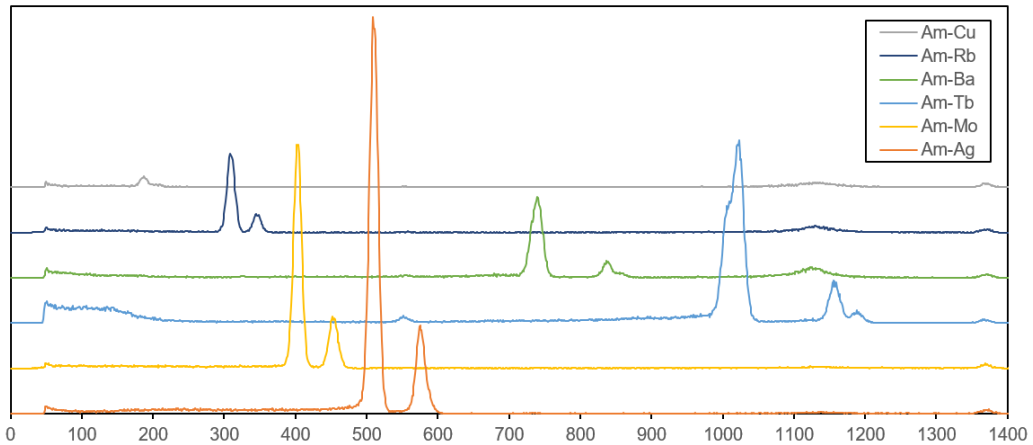


Figure 10: ^{241}Am variable x-ray target material stacked plot (channel number on x-axis)

4.1.3 ^{241}Am Annular Source

The variable x-ray source was then removed and the following samples were loaded (at distances quotes from the detector window) in conjunction with the annular ^{241}Am source (Figure 6):

- Sample foil "TiF", 60mm distance.
- Source only, no sample, 60mm distance.
- Sample "u1", 60mm distance.

The source only sample was taken so that each sample spectra may be subtracted from the source only one, thus presenting the peaks present due to the sample only (mostly). Figure 11 shows the spectra obtained and alongside the additional subtractions. The spectrum for the foil (Figure 7) shows no noticeable any change from the source only spectrum in the 0-60 keV range, the peak fitting analysis and further interrogation may reveal peaks with lower intensities than visible from the direct ASCII plots. Sample u1 produces the most noticeable response, with two large peaks (one within the other) present at ~ 10 keV. Further analysis is clearly required in order to determine elemental composition from these three samples.

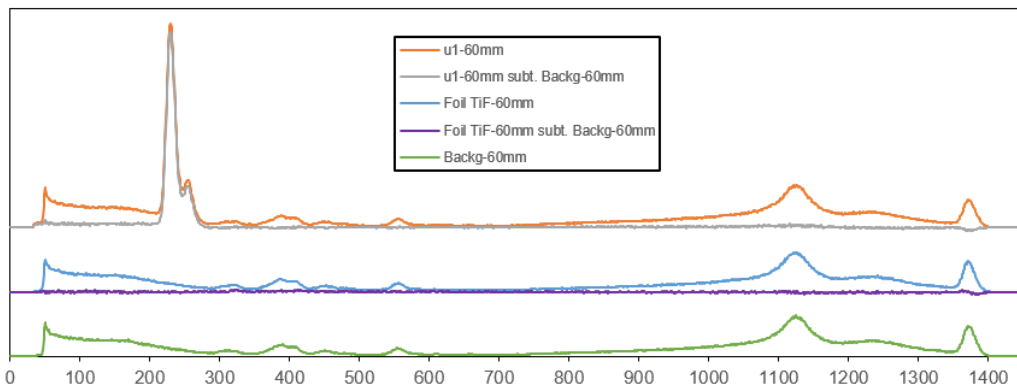


Figure 11: ^{241}Am annular source stacked plot (channel number on x-axis)

4.2 Data Extraction

4.2.1 Reference Photon Energies

An MS Excel spreadsheet was set-up and photon energies and intensities were retrieved from Firestone table of isotopes [5] and the H.R. Verma [19] paper, for the relevant target materials (Appendix B) and for both ^{241}Am and ^{237}Np . Where there are a significant number of energies within a ~ 5 keV range, the weighted means were taken of the various photon energies using the relevant intensities. The resultant energies are the weighted mean energies used herein. For verification, the target $K\alpha$ and $K\beta$ energies of the variable x-ray source supplied via Appendix B were compared with the weighted mean energies ascertained through calculation and retrieved from Firestone et al [5].

4.2.2 Gaussian Fitting

Equations from the Louis Lyons book [11] were used to conduct linear fitting, non-linear fitting and error propagation. Each of the locally saved ASCII spectra were transferred onto the university PHYMAT Linux server. The ROOT software was loaded on the command window and the peaks of each spectra were then fitted using the Buffit.C fitting macro. Peaks that were clearly significant and resolvable (>1000 counts) within the spectra were fitted, although this rule was not absolute and a number of peaks with lower counts were also fitted out of interest. The output of the each peak fit gives a plot and data display consisting of the following data relevant to the peak(s); peak centroid, full-width half maximum, counts, intercept and slope. The fit error, step size and first derivative were also provided for each parameter. This data was copied and pasted into MS Excel for each fit, the text-to-columns function was then used to organise the data for analysis. The resultant Gaussian

fit is to be considered significant if the probability of a larger value of χ^2 is greater than the critical value of χ^2 at a significance (α) of 0.025 (two-tailed). Here the null hypothesis may be rejected and the results were not down to mere chance, however caution should still be taken, this measure does not prove that the results are correct explicitly. Using MS Excel, for a lower-tail one-sided test, the formula "CHISQ.DIST.RT(χ^2 ,Ndf)" is used, where χ^2 and the number of degrees of freedom is given by Buffit. If $P(\chi^2) < \alpha$ then the null hypothesis may be rejected. Failing to reject this test could be due to a number of factors, such as failing to attain a sufficient number of counts in a peak, or two or more peaks hidden within one (not resolved).

4.2.3 Energy Calibrations

The centroid positions of the fitted peaks plotted against known weighted mean energies should give a straight line correlation [8]. The resultant equation of the straight line allows the energy of unknown peaks to be predicted and subsequently characterised. Weighted least-squares straight line fits were conducted for both the ^{241}Am stick source and the ^{241}Am variable x-ray source. The actual error given by the Buffit Gaussian fit is overestimated in this case and not the actual error on the centroid. A least weighted squares fit was conducted in MS Excel, using the equations stated within Lyons [11], to estimate the errors and scale them accordingly. For a known straight-line weighted least squares fit, χ^2 should equal the number of degrees of freedom (NDf) (almost exactly) as there is a known straight-line relation between the weighted mean energy and centroid position. The fit error given by the Gaussian peak fitting is overestimated and is not the true error of the centroid positions, the true error was found by setting the value of χ^2 to the number of degrees of freedom (as explained above), this was done by creating a 'scale factor'. This scale factor was then used to estimate the actual errors on the centroid positions. The equation of these fits (Figures 12 and 13) may now be used to identify the peaks within the spectra captured by characterising them with an estimated energy and associated error.

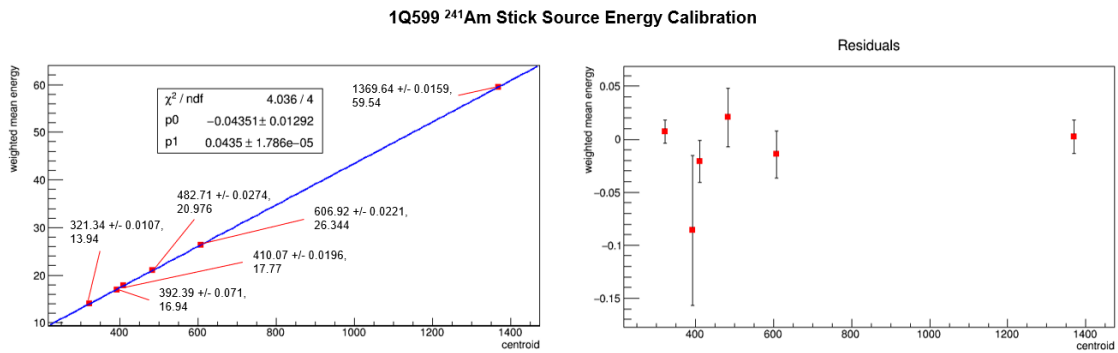


Figure 12: ^{241}Am stick source energy calibration

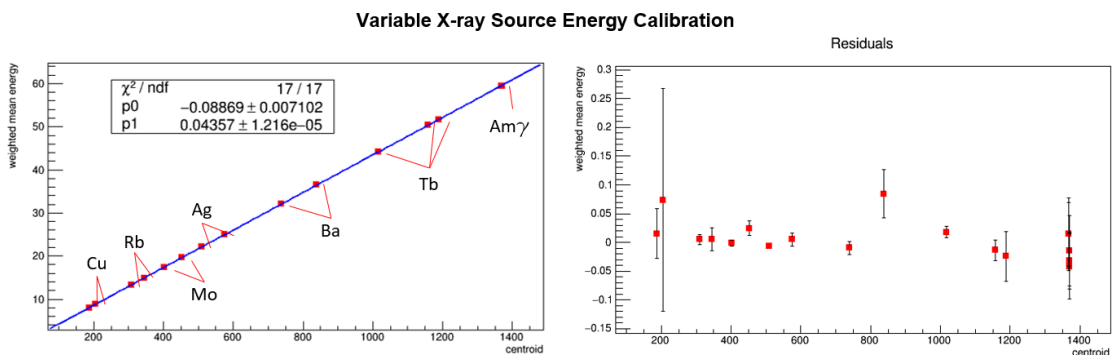


Figure 13: Variable x-ray source energy calibration

5 Results and Analysis

The majority of the resolvable peaks were the higher energy and more intense K α s and K β s. Only the L α , L β and L γ peaks of the 1Q599 ^{241}Am source were resolvable. Energies were fitted using the calibration data shown by Figures 12 and 13. Errors on the energies fitted were found by the using the general error propagation formula, as detailed within Lyons [11]. Table 4 details some of the key properties derived from the measurements and subsequent linear fits. All uncertainties tend to fall within the weighted mean energies, however there were exceptionally high uncertainties on the unknown peaks and on the two ~ 8 keV lines on the Cu target. The 59.5 keV ^{241}Am γ 's were fitted on the variable x-ray spectra and used in the energy calibration, but are not of concern for this table.

Source	Element	Z	Measured Energy (keV)	Uncertainty	Origin	W.M.Energy
1Q599	^{237}Np	93	13.936	0.390	L α 1	13.942
1Q599	^{237}Np	93	17.026	1.660	L β 1	16.94
1Q599	^{237}Np	93	17.795	0.544	L β 1	17.77
1Q599	^{237}Np	93	20.955	0.699	L γ 1	20.98
1Q599	^{241}Am	95	26.359	0.592	γ	26.345
1Q599	^{241}Am	95	59.539	0.476	γ	59.541
Var.X	Tb	65	23.994	1.213	Unk	Unk
Var.X	Tb	65	44.198	0.286	K α	44.216
Var.X	Tb	65	50.344	0.445	K β	50.331
Var.X	Tb	65	51.714	1.000	K β	51.690
Var.X	Rb	37	13.370	0.265	K α	13.375
Var.X	Rb	37	14.974	0.483	K β	14.980
Var.X	Rb	37	49.174	2.517	Unk	Unk
Var.X	Mo	42	17.444	0.206	K α	17.443
Var.X	Mo	42	19.657	0.330	K β	19.672
Var.X	Cu	29	8.026	1.006	K α	8.041
Var.X	Cu	29	8.831	4.446	K β	8.905
Var.X	Cu	29	49.133	3.049	Unk	Unk
Var.X	Ba	56	32.070	0.307	K α	32.060
Var.X	Ba	56	36.448	0.980	K β	36.533
Var.X	Ba	56	48.881	1.859	Unk	Unk
Var.X	Ag	47	22.109	0.191	K α	22.103
Var.X	Ag	47	25.002	0.300	K β	25.007

Table 4: Measured and fitted energy data.

5.1 Examination of Detector Properties

The majority of the observable peaks within an ^{241}Am spectrum where characterised at measurement using Knoll [8] and are generally well known. This source was used for ascertaining the detector properties as it provides is a reliable (known) control sample. Section 2.1 outlines the detector properties of interest and the equations followed for this procedure. The plot of log resolution against log energy (Figure 14) tends to indicate that the inclusion of the 59.5 keV ($\text{Am}\gamma$) data point brings the slope closer to a value of -1, where the result is dominated by noise as opposed to following Poisson statistics. With this point excluded, the slope of the straight line plot comes closer to a value of -0.5. The adverse effect of the higher energy data point is as expected full peak efficiency drops above a value of ~ 30 keV, as predicted in section 2.1. Error bars were not included as the fit errors were overestimated. This effect is confirmed in the following plot (Figure 15) which shows a drop-off in efficiency (intrinsic) with the inclusion of the higher energy 59.5 keV ($\text{Am} \gamma$) data point, illustrating concurrence with Figure 1 [8] and of similar results presented by Ben Abdelouahed et al [2].

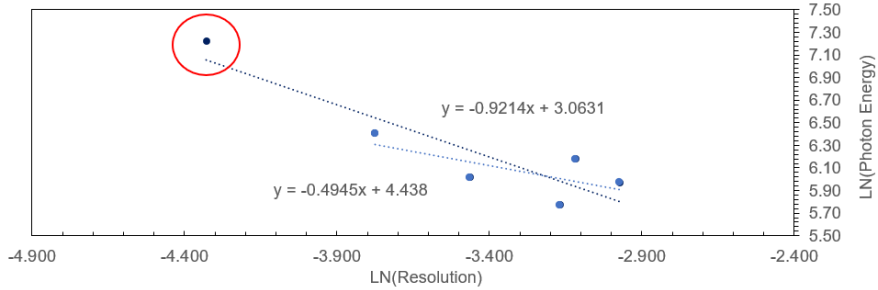


Figure 14: Plot of Log(Energy) against Log(Resolution)

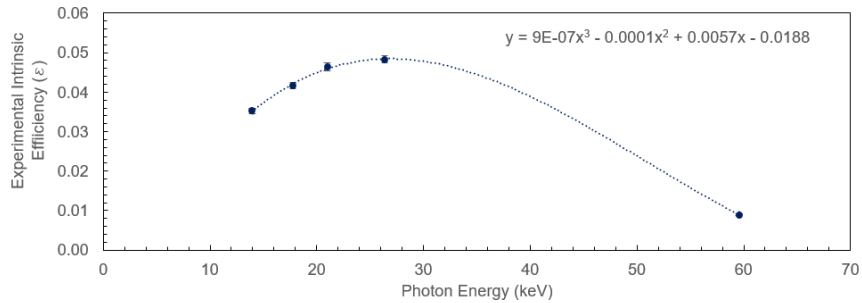


Figure 15: Plot of efficiency against measured photon energy (keV).

5.2 Moseley's Law

The results presented on Table 5 are those calculated for the Moseley's law investigation. The errors ascertained by forcing $\chi^2 = \text{Ndf}$ are an order of magnitude greater than the errors predicted from the centroid fits (as provided by Buffit). The scaled errors are clearly being over-estimated in order to fit a straight line through the plots, this indicates that the relation between the atomic number of element (Z) and the square-root of the measured centroid positions (photon energies) is not as linear as it may first appear. The robust estimates (provided the Buffit fitting) of the centroid positions should clearly be used and the resultant χ^2 statistic may be used to evaluate the fit.

Sqrt Centroid (x)	Scaled Errors $\sigma(x)$	Buffit Errors $\sigma(x)$	Z	Origin	Element
31.883	0.050	0.00092	65	Ka	Tb
17.576	0.081	0.00148	37	Ka	Rb
20.060	0.042	0.00078	42	Ka	Mo
13.647	0.494	0.00905	29	Ka	Cu
27.168	0.510	0.00936	56	Ka	Ba
22.572	0.030	0.00055	47	Ka	Ag
34.023	0.091	0.00151	65	Kb	Tb
34.482	0.214	0.00356	65	Kb	Tb
18.594	0.183	0.00305	37	Kb	Rb
21.284	0.101	0.00168	42	Kb	Mo
14.308	2.319	0.03867	29	Kb	Cu
28.959	0.249	0.00415	56	Kb	Ba
23.998	0.078	0.00130	47	Kb	Ag

Table 5: Moseley's law results

The resultant $K\alpha$ and $K\beta$ fits are shown on Figure 16. The second (34.382) $K\beta$ of Terbium looks to be acting as an outlier to the straight line fit. Visually, the lines appear to be good fits. Even so, the χ^2/NDF values of 11891/4 ($K\alpha$) and 17971.2/5 ($K\beta$) illustrates that there is no evidence to suggest that this data follows a straight line. These values correspond to a negligible probability. Although if larger error estimates were present, then

the data could indeed be represented by a straight line. There is clearly non-random behaviour in both $K\alpha$ and $K\beta$ residual plots which further illustrates that the data is not well-represented by a straight line fit.

The final value to investigate is the rest mass of an electron, the resultant value may then be compared to the well-known value of $511 \text{ keV}/c^2$ [8]. Equation 5 may be re-arranged to find this for Moseley's Law. For both the $K\alpha$ and $K\beta$ x-rays, an averaged value of $524.86 \text{ keV}/c^2 +/ - 15.78 \text{ keV}/c^2$ was found. This is more than 0.87 standard deviations from the expected value, within the lower error bounds, but not very precise. The theory behind Moseley's law is inaccurate when looking at this data-set, especially so as Z increases. From the data obtained (Appendix E) it can be seen that, for $K\alpha$, the fitted (measured) x-ray energy (and Z) increases from $8.11 \text{ keV} \rightarrow 45.05 \text{ keV}$, as does the solution for the electron rest mass $512.36 \text{ keV}/c^2 \rightarrow 540.08 \text{ keV}/c^2$. For $K\beta$ the solutions for the rest mass starts closer to the $511 \text{ keV}/c^2$ value but ends at $Z = 65$, higher than expected.

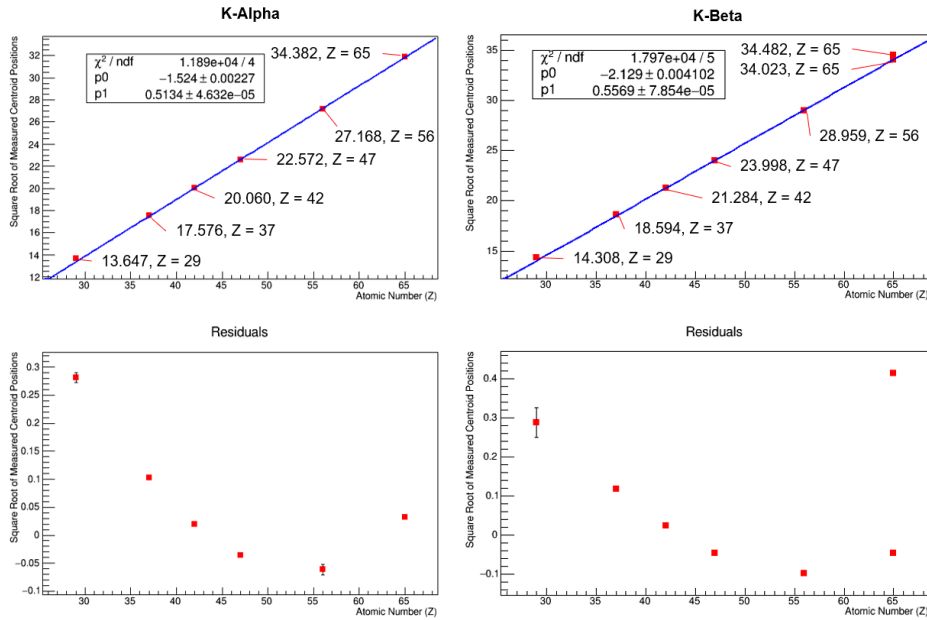


Figure 16: Moseley's law fit of measured energies against atomic number

An improved model, which attempts to approximate relativistic affects shall be now utilised. The Bohr-Sommerfeld fit (Equations 6 and 7) residuals were then plotted for both $K\alpha$ and $K\beta$ x-rays (Figure 17). This plot clearly still shows a non-random pattern with residual increasing with atomic number (Z). The χ^2/NDF values are much improved over Moseley's law and are $481.2/4$ ($K\alpha$) and $8.38/5$ ($K\beta$). An odd trend here to point out is that this statistic is now relatively worsened for $K\alpha$ (negligible significance) but improved for $K\beta$ (now a 13.6% probability) opposing the findings earlier for Moseley's law. The results for $K\beta$ in this case are not rejected. S tends to increase drastically as with atomic number (Z) which again indicates that this fit is becoming increasingly inaccurate as with increasing atomic number (Z). The errors on the Copper $\sim 8 \text{ keV}$ x-rays are still excessive, possibly due to fit errors.

The final investigation for the Bohr-Sommerfeld approximation is the rest mass of an electron. For both the $K\alpha$ and $K\beta$ x-rays, an averaged value of $505.42 \text{ keV}/c^2 +/ - 7.53 \text{ keV}/c^2$ was found. This is only 0.75 standard deviations from the well known value of 511 keV , more precise as before, and within the error found. On this occasion however (Appendix E) as the measured $K\alpha$ x-ray energy increases from $8.11 \text{ keV} \rightarrow 45.05 \text{ keV}$ the solution for the electron rest mass decreases from $505.61 \text{ keV}/c^2 \rightarrow 501.33 \text{ keV}/c^2$. For $K\beta$ the solution follows the same trend, with the exception of the $K\beta 2$ of Terbium (energy $\sim 51.7 \text{ keV}$) which increases to $516.18 \text{ keV}/c^2$.

The above evidence seems to suggest that a fully relativistic model is the most accurate one. As mentioned in Section 2.4.1, the approximations of electron shielding (σ) used within both models may not be appropriate as suggested by Whitaker et al [20]. Equation 5 was re-arranged to find the shielding factor (σ), assuming a

fixed value of the electron rest mass of $511 \text{ keV}/c^2$. Across the range of measured energies the results were plotted and are shown on Figure 18. From the findings the screening factor becomes more constant in the fully relativistic Bohr-Sommerfeld case, increasing slightly (adverse behaviour) at heavier atomic masses. In the case of Moseley's law, there is a severe reduction away from the values of $(K\alpha)$ 1 and $(K\beta)$ 2 whereby the value becomes negative for $K\alpha \gtrsim 55$. There should be clearly be an element of atomic fine structure at all atomic weights, moreover at higher atomic masses, where (in a classical sense) the electron would be moving at increasingly greater fractions of the speed of light. Of course this would be more appropriately expressed as a function of electron binding energy tending towards the mass of the electron. The consequence of thus could affect the shielding factor in this way.

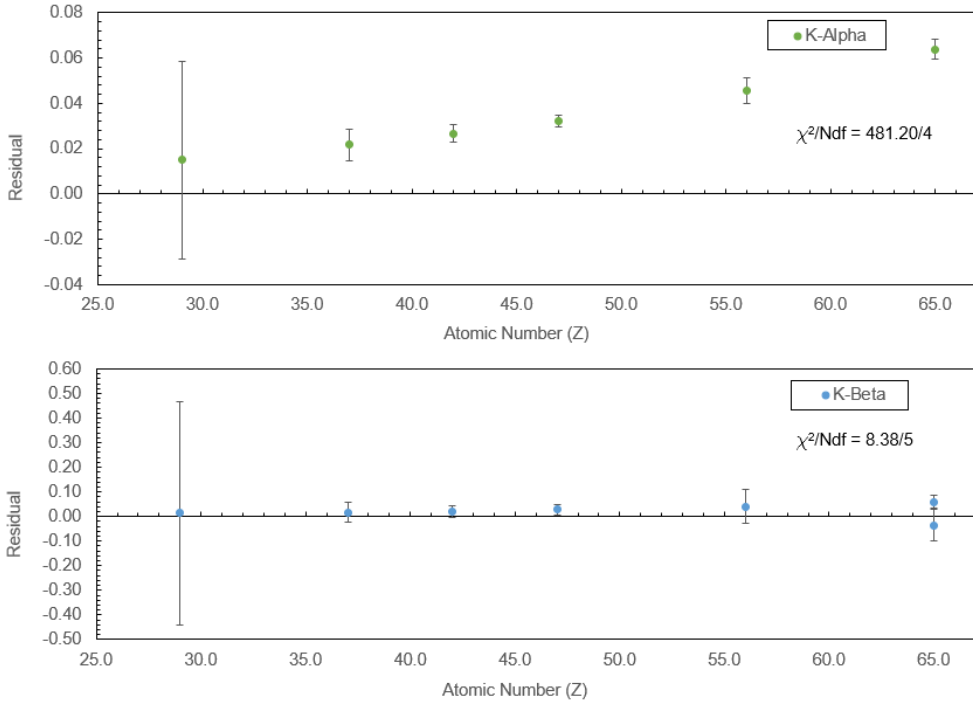


Figure 17: Bohr-Sommerfeld residuals plot

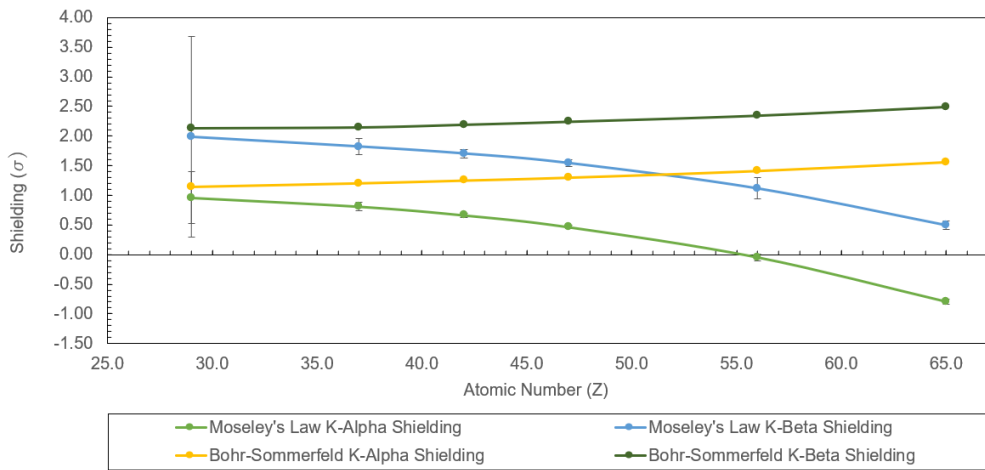


Figure 18: Electron shielding against atomic number for both the Moseley and the Bohr-Sommerfeld models

5.3 Application of Theory - Unknown Samples

A series of L- series x-rays were retrieved using the energy library created in Section 4.2.1 [5] given that the only measured L-series x-rays were from a single atomic weight (Neptunium). This produced an approximate L α and L β model to place the measured energies from the unknown samples upon. At this point, ideally, atomic number could then be solved. As previously mentioned however, the Moseley's and Bohr-Sommerfeld approximations become less accurate at higher atomic numbers. And instead of solving a complex set of equations for an approximate atomic number - in this case a reference plot (Figure 19) will be used visually. Whereby the author simply places the square root energy values from the unknown energies recorded on the plot, to see if the point lands on the K or L α or K or L β lines, the approximate atomic number can then be read-off on the x-axis. In order to confirm which line this lies on, the NIST x-ray database [14] was used to search for the measured/fitted energy (including error) and confirm the transition and element.

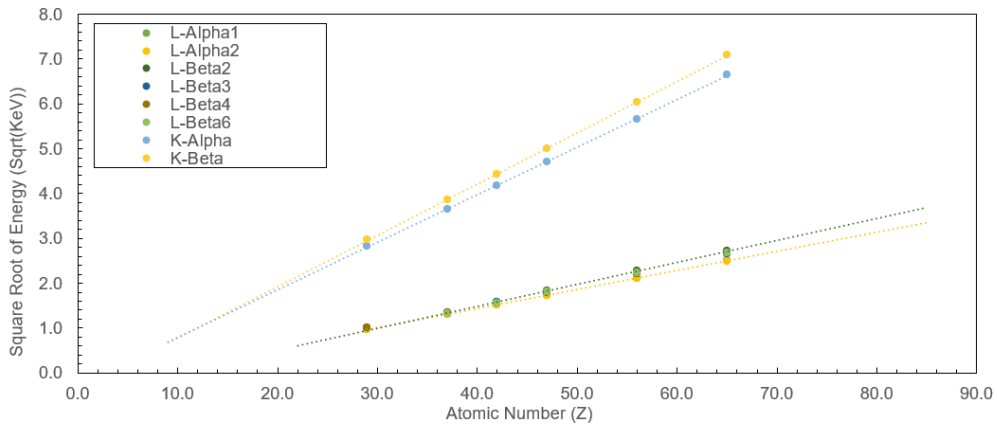


Figure 19: Reference plot

5.3.1 Sample "u1"

The two major peaks (visible on Figure 11) are shown fitted on Figure 20. The value of the \sqrt{E} energy for the largest peak (left) is 3.156 (9.95 keV) \pm 0.0022, the smaller peak (right) is 3.3095 (10.95 keV) \pm 0.0022. A read off on Figure 20 gives an atomic number (Z) around 32 on the K α or β . As there are two major peaks only and they are the most intense, at this energy they are likely to be the K α and K β of Germanium (Z = 32). The sample therefore may be a relatively pure form of Germanium. This sample is also silvery in appearance and conforms to other observational findings corresponding to Germanium.

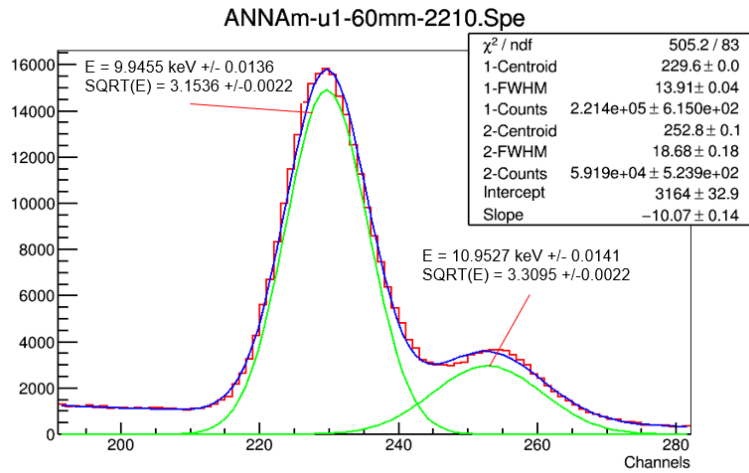


Figure 20: Sample "u1" peaks of interest

5.3.2 Sample "TiF"

No readily resolvable peaks were available on this spectra with which the above method may be employed. This sample illustrates the requirement for more accurate methods of determination i.e. background subtraction, dedicated software to determine peak origin and compositions, vacuum conditions, etc.

6 Conclusion

These results show an number indications that Moseley's law does not hold true and illustrates a bad fit against a least-squares linear fit, with χ^2 much greater than just noise for the number of degrees measured. This is also simply an analytical error and real errors also add to this, there is also evidence of non-random behaviour in the residuals plot. The Bohr-Sommerfeld relativistic correction gives a much improved fit, with χ^2 reduced drastically, but still greater than what would be expected for experimental error/noise. Results were tested against the known value of the rest mass of an electron ($511 \text{ keV}/c^2$) [8]. Moseley's formulae gave $524.86 \text{ keV}/c^2 +/- 15.78$ and the Bohr-Sommerfeld approximation gave $505.42 \text{ keV}/c^2 +/- 7.53$. Clearly the shielding factor (σ) is more complex than predicted and changes as atomic number (Z) increases. In the classical sense, the velocity of orbital electrons tends toward the speed of light (c) with increasing atomic number and the affect of shielding cannot be considered without some level of correction for this.

In summary, Moseley's law is an inaccurate representation of the data, and although the relativistic correction is much improved, more modern fine structure theories of the atom show that the underlying assumptions of the time were false. In more recent times, the study of quantum mechanics has led to the current theory that electrons exhibit wave-particle duality, experiments such as the two slit diffraction help to illustrate thus. Modern fully-relativistic solutions of Dirac and of the non-relativistic solutions of Schrodinger may technically give better solutions, but maybe actual experimental errors would mean that these solutions are not worth doing. Practically, more specialised equipment could be applied to improve the accuracy of x-ray fluorescence techniques, particularly for more complex compounds with varying compositions. The fact that Moseley's discoveries are still relevant today illustrates the importance of the work, which is an astonishing discovery for the time - worthy of the highest honour. There is no doubt that Henry would have gone on to contribute so much more in this field, but sadly, as with many of his age at the time, he paid the ultimate sacrifice in the line of duty.

6.1 Further Work

The L-Series x-rays were not fitted in this case, further work could be done in order to clean this part of the spectrum, capture and investigate these peaks. In-particular attempting to measure the energies of the Lt and Ls x-rays from ^{237}Np as detailed by Verma et al [19]. Further work is clearly required to identify the unknown sample "TiF", although the sample "u1" demonstrates the application well. More work is required to explore newer models in order to explain the characteristic x-rays fluoresced from these and higher atomic mass elements.

References

- [1] Amptek. *X-Ray Fluorescence (XRF): Understanding Characteristic X-Rays*. URL: https://www.amptek.com/-/media/ametekamptek/documents/resources/tutorials/characteristic_xrays.pdf?la=en&revision=8986f72c-3819-4fd3-867c-bb4854c518e4. Date Accessed: 14 December 2021.
- [2] Haifa Ben Abdelouahed, Omrane Kadri, and Adel Trabelsi. “Si(Li) detector parameters optimization using efficiency calibration”. In: vol. 935. Mar. 2007. DOI: 10.1063/1.2795418.
- [3] University of Birmingham Dept. of Physics and Astronomy. *Source Activities*. URL: <https://canvas.bham.ac.uk/courses/60469/pages/source-activities>. Date Accessed: 18 December 2021.
- [4] W.E. Burcham and M. Jobes. *Nuclear and Particle Physics*. Nuclear and Particle Physics. Longman, 1995. ISBN: 9780582450882. URL: <https://books.google.co.uk/books?id=Ob-HAQAAACAAJ>.
- [5] Richard B Firestone, Coral Baglin, and S Y Frank Chu. *Table of isotopes: 1998 update with CD-ROM*. New York, NY: Wiley, 1998. URL: <https://application.wiley-vch.de/books/info/0-471-35633-6/toi99/toi.htm>.
- [6] M.A. H.G.J. Moseley. “XCIII. The high-frequency spectra of the elements”. In: *The London, Edinburgh, and Dublin Philosophical Magazine and Journal of Science* 26.156 (1913), pp. 1024–1034. DOI: 10.1080/14786441308635052. eprint: <https://doi.org/10.1080/14786441308635052>. URL: <https://doi.org/10.1080/14786441308635052>.
- [7] IUPAC. *Part VIII. Nomenclature system for X-ray spectroscopy (Recommendations 1991)*. URL: <http://old.iupac.org/reports/V/spectro/partVIII.pdf>. Date Accessed: 19 December 2021.
- [8] Glenn F. Knoll. *Radiation Detection and Measurement*. 3rd. New York, NY: Wiley, 2000. URL: <https://cds.cern.ch/record/441925>.
- [9] David W. Kraft. “Relativistic Corrections to the Bohr Model of the Atom”. In: *American Journal of Physics* 42.10 (1974), pp. 837–839. DOI: 10.1119/1.1987875. URL: <https://doi.org/10.1119/1.1987875>.
- [10] Kenneth S Krane. *Introductory Nuclear Physics*. New York, NY: Wiley, 1988. URL: <https://cds.cern.ch/record/359790>.
- [11] Louis Lyons. *A Practical Guide to Data Analysis for Physical Science Students*. Cambridge University Press, 1991. DOI: 10.1017/CBO9781139170321.
- [12] Miron. *SiLi Detector Detector Datasheet*. URL: https://mirion.s3.amazonaws.com/cms4_mirion/files/pdf/spec-sheets/c40120_sili_det_for_x-ray_spect_ss_2.pdf?1562601347. Date Accessed: 15 December 2021.
- [13] NHQ. *High Precision Single/Dual Channel HV Module in NIM Standards Brochure*. URL: https://iseg-hv.com/files/media/iseg_datasheet_NHQ_en_20210329082518.pdf. Date Accessed: 15 December 2021.
- [14] NIST. *Easy-MCA*. URL: <https://physics.nist.gov/PhysRefData/XrayTrans/Html/search.html>. Date Accessed: 20 January 2021.
- [15] ORTEC. *671 Amplifier Brochure*. URL: <https://www.ortec-online.com/-/media/ametekortec/brochures/6/671-a4.pdf?la=en&revision=461ed615-541a-43e8-a71c-385f888afe5c>. Date Accessed: 15 December 2021.
- [16] ORTEC. *Easy-MCA*. URL: <https://www.ortec-online.com/-/media/ametekortec/brochures/e/easy-mca-a4.pdf?la=en&revision=d4e5f46c-3e65-491a-a947-10cbaa5def05>. Date Accessed: 18 December 2021.
- [17] ORTEC. *Minibin and Power Supply Brochure*. 2021. URL: <https://www.ortec-online.com/-/media/ametekortec/brochures/4/4006-a4.pdf?la=en&revision=75400194-483b-40e6-ab52-ca166bf25a8>. Date Accessed: 15 December 2021.
- [18] Tomas Soltis, Lorcan M. Folan, and Waleed Eltareb. “One hundred years of Moseley’s law: An undergraduate experiment with relativistic effects”. In: *American Journal of Physics* 85.5 (2017), pp. 352–358. DOI: 10.1119/1.4977793. URL: <https://doi.org/10.1119/1.4977793>.

- [19] H.R. Verma. “Measurements of M and L X-ray energies and relative intensities emanating from ^{241}Am source”. In: *Applied Radiation and Isotopes* 122 (2017), pp. 41–46. ISSN: 0969-8043. DOI: <https://doi.org/10.1016/j.apradiso.2017.01.005>. URL: <https://www.sciencedirect.com/science/article/pii/S0969804316303657>.
- [20] M A B Whitaker. “The Bohr-Moseley synthesis and a simple model for atomic x-ray energies”. In: *European Journal of Physics* 20.3 (Jan. 1999), pp. 213–220. DOI: 10.1088/0143-0807/20/3/312. URL: <https://doi.org/10.1088/0143-0807/20/3/312>.

Bibliography

W.E. Burcham and M. Jobes. *Nuclear and Particle Physics*. Nuclear and Particle Physics. Longman, 1995. ISBN: 9780582450882. URL: <https://books.google.co.uk/books?id=0b-HAQAAACAAJ>.

Richard B Firestone, Coral Baglin, and S Y Frank Chu. *Table of isotopes: 1998 update with CD-ROM*. New York, NY: Wiley, 1998. URL: <https://application.wiley-vch.de/books/info/0-471-35633-6/toi99/toi.htm>.

Glenn F. Knoll. *Radiation Detection and Measurement*. 3rd. New York, NY: Wiley, 2000. URL: <https://cds.cern.ch/record/441925>.

Kenneth S Krane. *Introductory Nuclear Physics*. New York, NY: Wiley, 1988. URL: <https://cds.cern.ch/record/359790>.

Louis Lyons. *A Practical Guide to Data Analysis for Physical Science Students*. Cambridge University Press, 1991. DOI: 10.1017/CBO9781139170321.

Appendix A

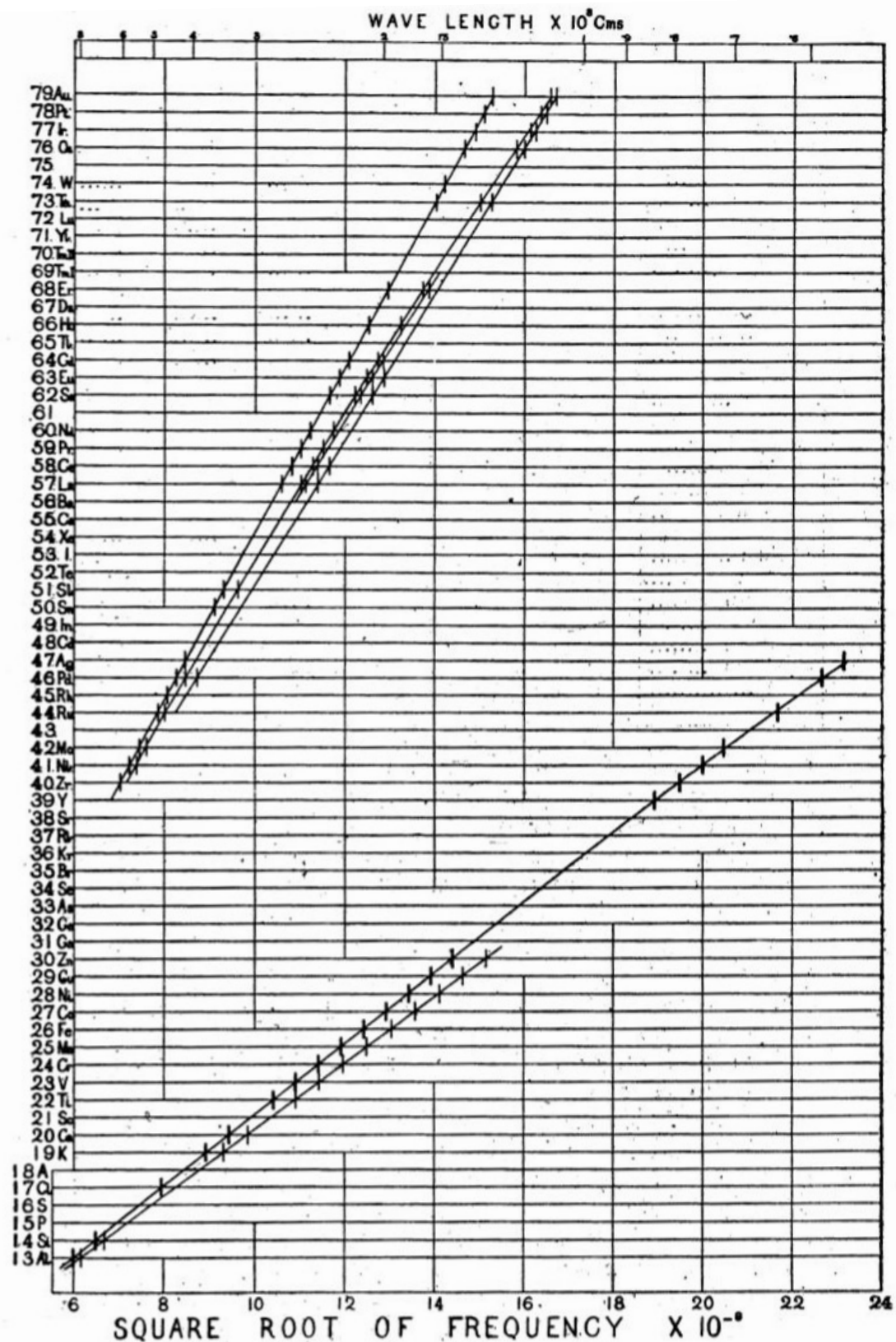


Figure 21: Moseleys Law [6]

Appendix B

Amersham International Limited
White Lion Road Amersham
Buckinghamshire England HP7 9LL

C3 LAB

Product specification

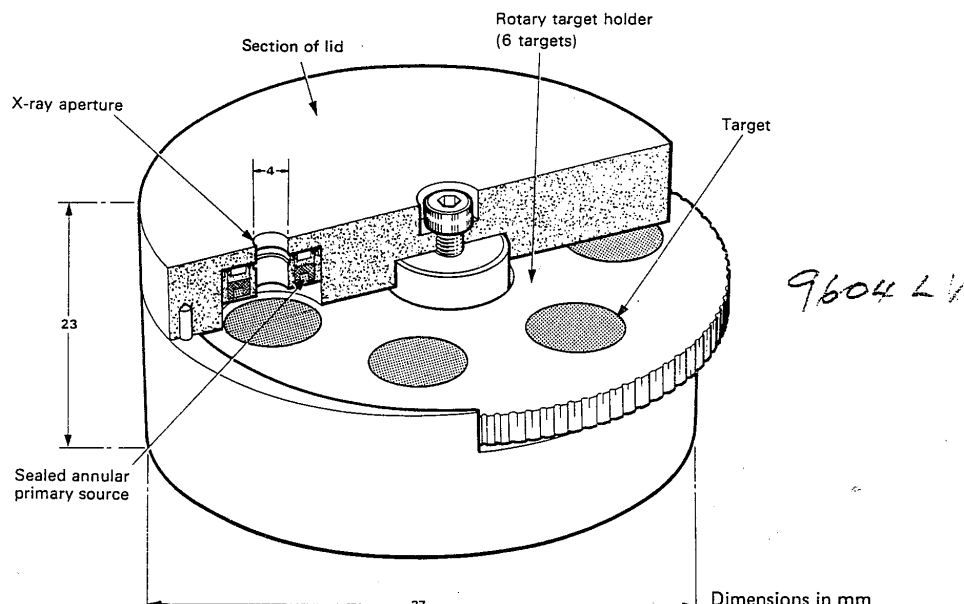
Variable energy X-ray source
code AMC.2084

Data
sheet
11196

SPECIFICATION

Construction:

A compact assembly containing a sealed ceramic primary source which excites characteristic X-rays from six different targets in turn. The annular primary source surrounds the X-ray emission aperture in the fixed part of the stainless steel assembly and the targets are mounted on a rotary holder. Each target can be presented to the primary source in turn and the characteristic X-rays from the target are emitted through the 4mm diameter aperture.



Primary source:

A 10mCi americium-241 source, consisting of a ceramic active component in a welded stainless steel capsule, with integral tungsten alloy rear shielding.

X-ray emission:

Target selected	Energy (keV) (1)		Intensity (2)	Photon yield (2)
	K _α %	K _β %		(photons/sec per steradian)
Cu	8.04 150	8.91 17		2,500
Rb	13.37 150	14.97 24		8,800
Mo	17.44 150	19.63 28		24,000
Ag	22.10 151	24.99 30		38,000
Ba	32.06 152	36.55 34		46,000
Tb	44.23 153	50.65 38		76,000

Notes: (1) weighted mean energies.

(2) the photon yield has been determined using a high resolution Si (Li) X-ray spectrometer (the values listed amend those shown in the 1974/5 catalogue); the photon output is highly collimated limiting emission to ~0.5 steradians.

Maximum surface dose rate: (excluding emission aperture where the dose rate will vary with the target in use) <0.1mR/h (as measured with type NIS295 gamma dose rate meter which has a flat energy response from 45keV to 2.5MeV.)

Amersham

NUCLEAR DATA — Americium-241

Half life: 433y
principal α -energies: 5.442 (12.5%); 5.484 (85.2%)
 γ -energies: 59.5keV (35.3%)
and others in low abundance
X-ray energies: Np L X-rays, 11.9 — 22.2keV.

QUALITY CONTROL

(all tests are applied to the primary source)

- Surface contamination:** the source is wiped with a swab moistened with ethanol or water; the activity removed is measured.
Limit: 0.005 μ Ci
- Leak test:**
- (i) the source is immersed in water at 50°C for 4 hours and the activity in the water is measured.
Limit: 0.005 μ Ci
 - (ii) the source is immersed in a suitable liquid (ethanediol) and the pressure in the vessel reduced to 100mm of mercury. No bubbles must be observed. (This test is described in Appendix B of B.S. 3513 : 1962).
- Special testing:**
- (i) the source has been tested and shown to comply with the IAEA 'special form' requirements (IAEA Safety Series No.6, 1967).
 - (ii) the source meets the requirements of the American National Standards Institute for calibration sources; class C54344 (United States of America Standards Institute, now the American National Standards Institute. Proposed classification of Sealed Radioactive Sources USASI Report N5.10, 1968).

A Test Report is supplied with each source.

IDENTIFICATION

Each assembly is engraved with the following:
Variable Energy X-Ray Source Serial No.
 ^{241}Am — 10mCi TRC, Year of manufacture.

AVAILABILITY

Sources are normally available from stock and can be despatched within one week of receiving an order.

PACKAGING

Each source is packed in a fitted wooden box which has appropriate labelling. The box is sealed in a metal container prior to despatch.

DOCUMENTATION

A copy of this Data Sheet together with a set of suggested experiments for educational use are provided with each source.

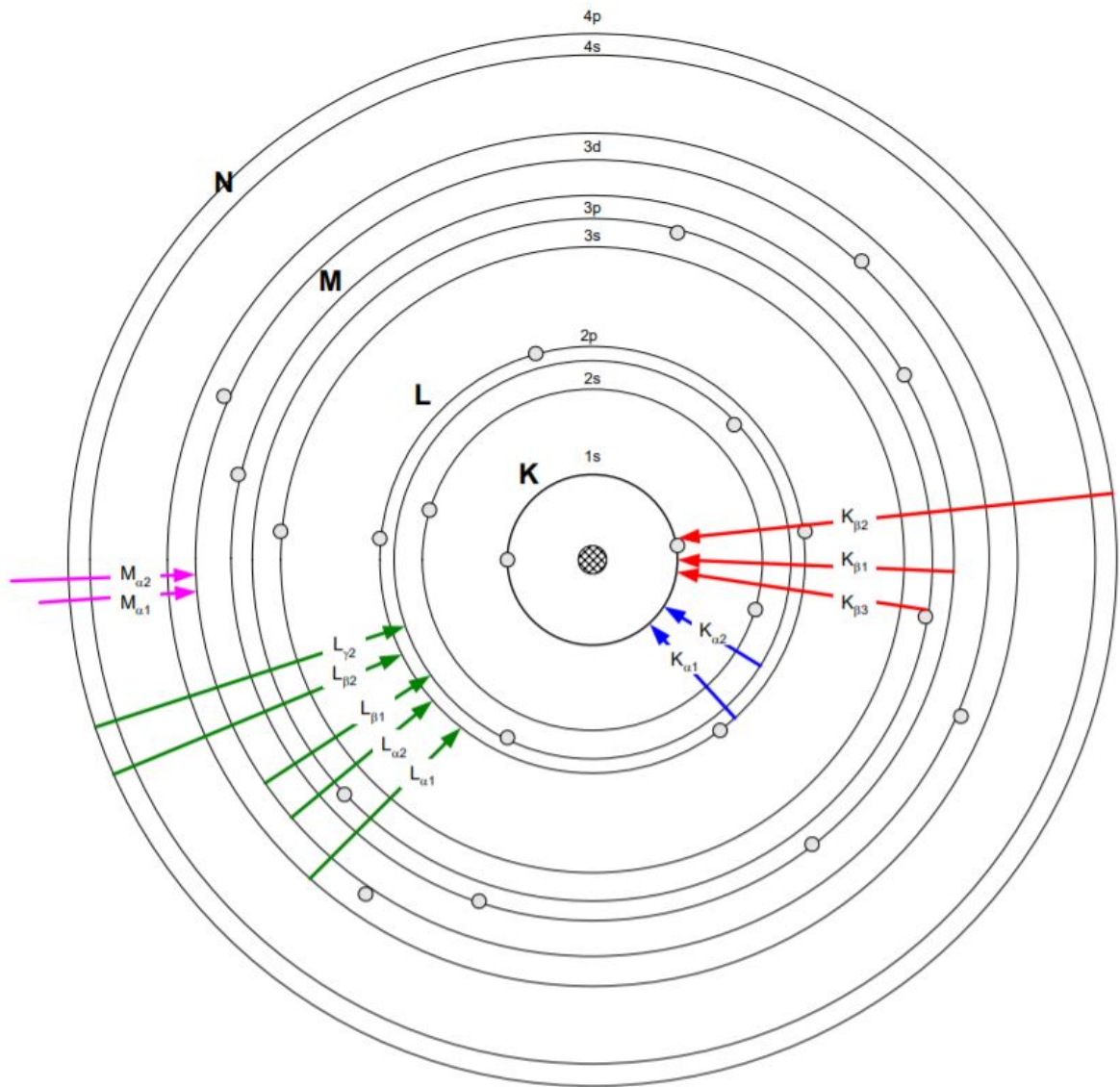
NOTE

No attempt should be made to dismantle the assembly or the primary source will be exposed.

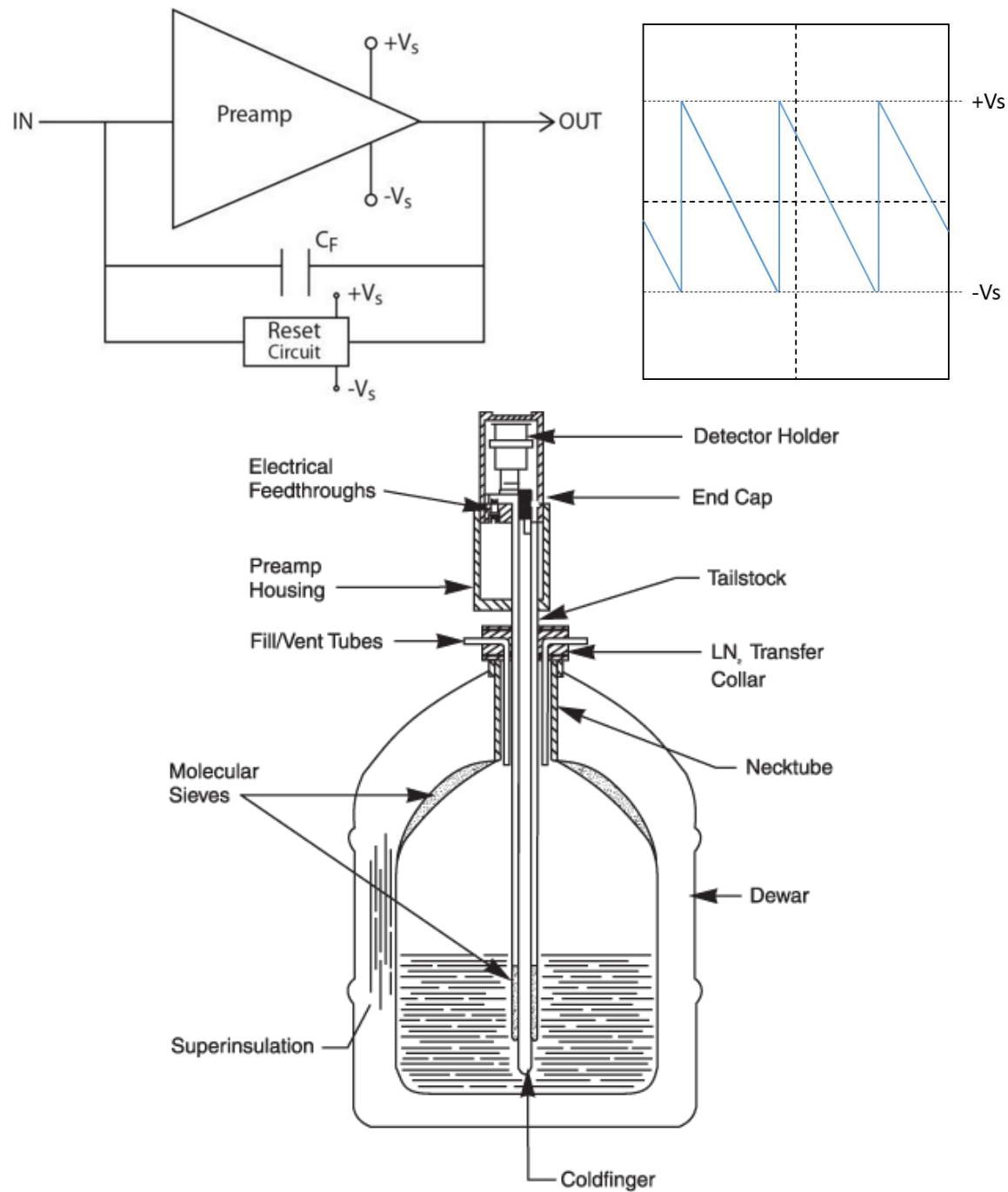
RELATED PRODUCTS

For applications requiring higher photon outputs of a single X-ray, fixed source/target assemblies are available. With these assemblies yields of up to 2×10^5 photons per second per steradian of Ag K X-rays can be obtained and even higher yields are possible using specially designed assemblies.

Appendix C



Appendix D



Appendix E

	Z	yfit Measured	yfit Error	Moseley keV/c²	Error	B-Som. keV/c²	Error
Ka	29.0	8.0257	0.2471	512.3634	15.7756	505.6147	15.5678
Ka	37.0	13.3670	0.0521	516.3367	2.0117	505.0260	1.9676
Ka	42.0	17.4435	0.0312	519.3697	0.9301	504.5442	0.9035
Ka	47.0	22.1091	0.0250	522.9559	0.5903	504.0646	0.5689
Ka	56.0	32.0696	0.0647	530.6129	1.0706	502.8945	1.0147
Ka	65.0	44.1985	0.0585	540.0789	0.7144	501.3322	0.6631
Kb	29.0	8.8312	1.1065	511.5811	64.0984	506.0118	63.4006
Kb	37.0	14.9739	0.1133	516.20568	3.9041	506.7031	3.8322
Kb	42.0	19.6473	0.0714	518.5680	1.8838	506.0394	1.8383
Kb	47.0	25.0022	0.0626	521.4069	1.3061	505.3745	1.2660
Kb	56.0	36.4481	0.24	527.8508	3.4848	504.1958	3.32866
Kb	65.0	50.3442	0.1029	535.6636	1.0950	502.4998	1.0272
Kb	65.0	51.7145	0.2456	550.2429	2.6134	516.1764	2.4516